Seed-Mediated Co-reduction: A Versatile Route to Architecturally Controlled Bimetallic Nanostructures
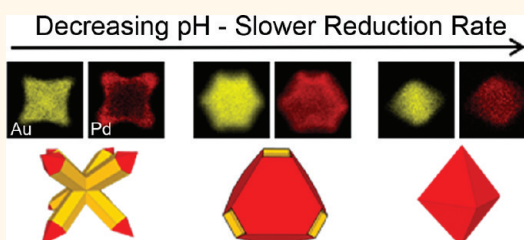
Christopher J. DeSantis, Aaron C. Sue, Matthew M. Bower, and Sara E. Skrabalak*

Department of Chemistry, Indiana University, Bloomington, Indiana 47405, United States

The construction of bimetallic nanostructures with defined composition, shape, and architecture is important to many applications.[1−3] For example, shape-controlled alloyed nanoparticles and binary metal nanodendrites can be more effective catalysts than their monometallic counterparts for electrooxidation processes.[4−8] Their enhanced performances are often attributed to the unique structure of the expressed surfaces and synergistic effects between the two metals that comprise the nanocrystals. Also, the optical properties of metal nanocrystals can be manipulated through the introduction of a second metal.[9−11] For example, core@shell and segmented bimetallic nanorods display surface plasmon resonances (SPRs) that are dependent on both their aspect ratios and composition.[12−14] Despite these examples, achieving the necessary synthetic control to access new bimetallic nanostructures with defined features is not always straightforward given the different properties of each metal and their precursors used in a nanocrystal synthesis. For example, metal precursors may be reduced at different rates during co-reduction and limit the nucleation of defined mono- or bimetallic seeds.[15,16] Also, structure-directing agents can interact preferentially with different metal surfaces.[17] Seed-mediated synthetic methods have the capacity to address some of the challenges associated with bimetallic nanocrystal synthesis, as nucleation is already accounted for by the seed.[18−21] As we report here, seed-mediated co-reduction of two metal precursors represents a potentially general route to architecturally controlled bimetallic nanocrystals, including octopodal and concave core@shell nanocrystals as well as new shape-controlled alloy and hopper-like nanostructures.

When seeds are incorporated into a nanomaterial synthesis, the barrier to deposition is typically lower than the nucleation of a new phase (i.e., heterogeneous versus homogeneous nucleation). This condition separates nanocrystal nucleation from growth, as the seeds represent preferential sites for the growth of the greater nanostructure. As a result, seed-mediated synthetic methods have the potential to yield nanocrystals with high degrees of precision and structural/compositional complexity.[18−22] For example, this method has been used to synthesize a variety of shape-controlled and core@shell metal nanocrystals as monodisperse samples (e.g., Au nanorods and those with high index facets expressed such as {730}-terminated Au@Pd tetrahexahedra and {221}-terminated Au@Pd trisoctahedra).[23−26]

ABSTRACT

Gold—palladium octopods and new concave and shape-controlled alloy nanostructures are synthesized by seed-mediated co-reduction, wherein two metal precursors are reduced in the presence of seeds that serve as preferential sites for the growth of the larger nanostructures. Here, the first comprehensive study of this technique is presented in a model Au—Pd system and provides insight into the mechanism of formation for these architecturally distinct nanocrystals. A systematic evaluation of synthesis conditions decoupled the roles of (i) Au:Pd precursor ratio, (ii) reaction pH, and (iii) capping agent concentration in morphology development. These factors provide control of growth kinetics and ultimately the morphology and composition of the final nanostructures. Significantly, elucidating the overgrowth processes during seed-mediated co-reduction will lead to the synthesis of other architecturally controlled bimetallic nanocrystals.

KEYWORDS: heteroepitaxial deposition · branched nanostructures · kinetic control · hopper crystals · concave nanocrystals · shape control

Typically only one metal precursor is reduced in the presence of the metal seeds. Yet we recently demonstrated that coupling the co-reduction of two metal precursors with the seed-mediated method manipulates the kinetics of seeded growth and in turn the morphology of Au−Pd nanocrystals.[27] In particular, architecturally distinct Au−Pd octopods (i.e., nanocrystals with eight branches) and concave core@shell Au@Pd nanocrystals were achieved. Since this initial demonstration, Han and co-workers synthesized convex Au−Pd hexahedral-like nanostructures by seed-mediated co-reduction.[28] Likewise, Xia and co-workers recently achieved Pd−Pt alloyed nanocages by coupling co-reduction and galvanic replacement during a seed-mediated synthesis.[8] Collectively, these results highlight the promise of this technique toward achieving unique bimetallic architectures. However, a greater understanding of how this method can be used to control morphology and composition is required to apply it to other bimetallic systems.

In the initial demonstration of this technique a double seeded approach was employed. First, tiny Au seeds (<10 nm) were prepared. Then, Au precursor (HAuCl$_4$) was reduced on top of the seeds to make larger Au nanocrystals, which are referred herein as Au cores. Finally, additional Au precursor and Pd precursor (H$_2$PdCl$_4$) were added to the Au core solution and reduced with L-ascorbic acid (L-aa) in the presence of cetyltrimethylammonium bromide (CTAB). The Au:Pd precursor ratio determined the final nanocrystal morphology. A series of control experiments found that the HCl released from the Pd precursor was integral to morphology control, with its concentration altering the rates of (i) metal precursor reduction with L-aa and (ii) likely Au core etching via Au(III)-CTAB complexes. The interplay between these two mechanisms at different reaction conditions accounted for the array of nanostructures observed. Palladium itself (in either its precursor state or reduced form) also contributed to structure formation. Thus, understanding the role of each synthetic component and how to manipulate these parameters during synthesis will expand our ability to predictably achieve architecturally distinct bimetallic nanostructures via seed-mediated co-reduction.

In this article, a comprehensive set of experiments is described that provide critical insight into the kinetic control achieved by coupling co-reduction of two metal precursors with the seed-mediated synthetic approach. First, the independent roles of the Au:Pd precursor ratio and reaction pH on nanostructure formation are elucidated by systematically altering each parameter. This study revealed general principles for new nanocrystal design by achieving, for example, shape-controlled alloyed nanocrystals through manipulation of nanocrystal growth kinetics during seed-mediated co-reduction. Second, the role of CTAB as a capping agent is evaluated. Manipulation of particle shape through the use of various capping agents is typically considered a thermodynamic means of structure direction, as facet-selective adsorbate interactions can alter the relative energies of the expressed surfaces.[29] Our study found that Br$^−$ either from CTAB or added extraneously plays a critical role during the overgrowth process but contributes to morphology development by temporally separating Au and Pd precursor reduction. In fact, manipulation of this parameter facilitated the growth of hopper-like nanocrystals with deep angular concavities on what would be the {100} facets of cuboctahedral nanocrystals otherwise. These results provide a greater understanding of seed-mediated co-reduction and will facilitate the synthesis of new bimetallic nanocrystals with well-defined and controllable properties.

RESULTS AND DISCUSSION

Synthetic Control of Au−Pd Nanostructures. The general protocol for coupling co-reduction with the seed-mediated synthetic technique is outlined in the introduction, and the details of this approach can be found in the Methods and Supporting Information, Table S1 and Figure S1. In the initial demonstration of this technique, the amount of Pd precursor was varied relative to Au precursor in the overgrowth solution at Au:Pd ratios of 1:X where X is 0.01, 0.1, 0.2, 0.5, 1.0, and 2.0. Scanning electron microscopy (SEM) images of the products obtained are shown in Figure 1 as column A. Branching and the formation of octopods are evident with the addition of even a small amount of Pd precursor (e.g., sample 1A). The tips of the octopods become flattened as the amount of Pd precursor increases relative to Au precursor (e.g., sample 3A versus 5A), and eventually concave core@shell architectures are adopted at very high Pd precursor concentrations (Figure S2). Given that these structures do not form in the absence of the seed-mediated method or when the Au and Pd precursors are reduced independently (Figure S3), it is interesting to understand how the co-reduction process contributes to this morphology development and can be controlled.

Our previous study discovered that the Pd precursor itself provides HCl to the reaction media as a function of concentration (i.e., H$_2$PdCl$_4$ is prepared in excess HCl from PdCl$_2$, and it also complexes as [CTA]$_2$PdBr$_4$ and related species under conditions similar to our synthesis, as reported by Berhault and co-workers).[27,30] Replacing H$_2$PdCl$_4$ with Na$_2$PdCl$_4$ during seed-mediated co-reduction accelerated the rate of precursor reduction and provided the high driving force required for new nanocrystal nucleation, with large metal flakes observed at high Na$_2$PdCl$_4$ concentrations. It was concluded that HCl from the Pd precursor provided control over morphology by
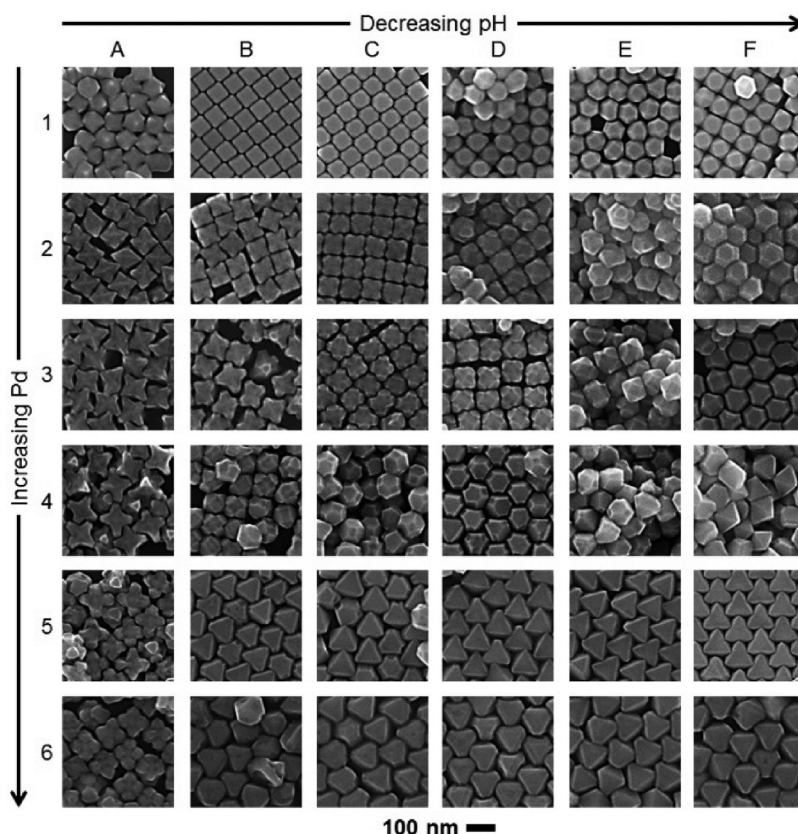
Figure 1. SEM images of Au–Pd nanocrystals synthesized by seed-mediated co-reduction. The synthetic results represented by columns A–F involved 2 mL of aqueous HCl solution being added to the Au core solution prior to co-reduction at concentrations of 0.0, 12.5, 25.0, 37.5, 50.0, and 62.5 mM, respectively. The synthetic results represented by rows 1–6 were obtained with Au:Pd precursor ratios of 1:X where X is 0.01, 0.1, 0.2, 0.5, 1.0, and 2.0 during co-reduction, respectively. See Tables S1 and S2 for a summary of synthetic conditions. Samples referred to by number-letter notation in the main text are based on this figure.

manipulating the kinetics of seeded growth. However, no additional studies were conducted to decouple the roles of reaction pH and Au:Pd precursor ratio in morphology development. Yet, experiments by Nishimura and co-workers have shown that the aspect ratio of Au nanorods can be controlled by the pH of the overgrowth solution, and similar observations have been made in other nanomaterial syntheses.[31−33] Thus, it is imperative to study the effect of reaction pH on morphology independent of the Au:Pd precursor ratio. This goal is achieved here by systematically adding different concentrations of HCl to the overgrowth solution prior to the co-reduction process at fixed Au:Pd precursor ratios. These results are also presented in Figure 1. The concentration of HCl added to the overgrowth solution increases from left to right in a row (A–F corresponds to 2 mL of 0.0, 12.5, 25.0, 37.5, 50.0, and 62.5 mM HCl added, respectively; the total reaction volume is 30.6 mL; see Supporting Information Table S2 for measurements of pH at different stages of synthesis), with each row corresponding to a different Au:Pd precursor ratio defined previously. Concave, cuboctahedral, and octahedral nanocrystals form in addition to the octopodal nanocrystals. These results

contrast with those obtained when the Au and Pd precursors are independently reduced in the presence of the Au cores and CTAB as a function of pH (Figure S3).

Examination of Figure 1 in more detail reveals some interesting trends. Across a given row nanocrystal size remains relatively constant, but branch lengths decrease and tips become flattened as HCl content increases (e.g., sample 4A *versus* 4B). Eventually, the nanocrystals adopt cuboctahedral or octahedral shapes (e.g., sample 4F). However, many of the intermediate samples contain concavities or depressions along specific facets (e.g., sample 4D). This trend toward convex solids is unsurprising, as decreasing pH slows the rate of metal precursor reduction and in turn nanocrystal growth. Slower growth allows nanocrystals to undergo relaxation processes and adopt thermodynamically favored morphologies rather than branched architectures.[34,35] Down a column, the overall size of the nanocrystals increases gradually with increasing metal content in the overgrowth solution. The tips of the branched nanocrystals also become flattened with increasing Pd precursor in the overgrowth solution, and cuboctahedral nanostructures with some concavities are observed (e.g., samples 2B, 3B, and 4B, respectively).
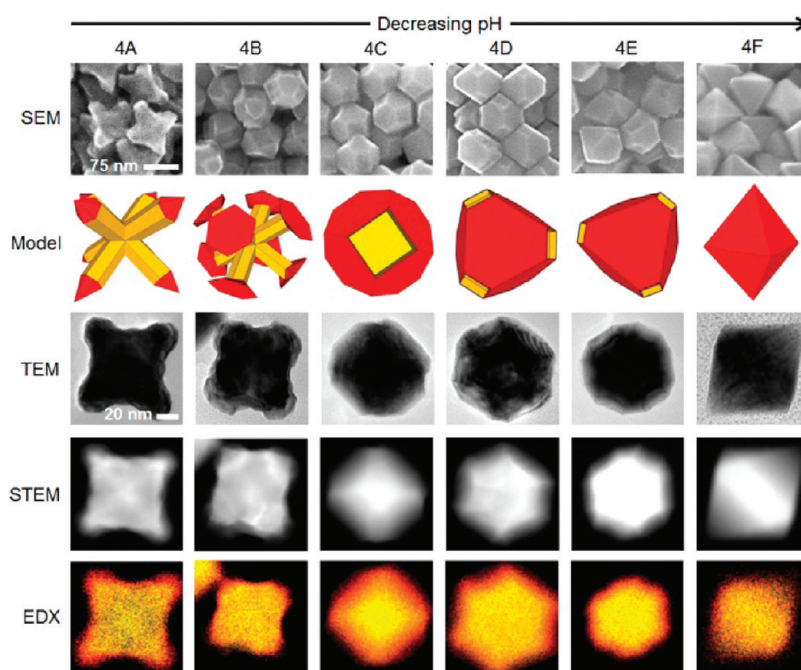
Figure 2. From top to bottom, Au−Pd nanocrystals (row 4, Figure 1) characterized by higher magnification SEM as well as 3-D models (yellow represents Au-rich and red represents Pd-rich regions), TEM, STEM, and STEM-EDX mapping (yellow indicates Au and red indicates Pd). Note: all SEM images are at the same magnification. Similarly, TEM, STEM, and STEM-EDX mapping are at the same magnification.

At sufficiently high concentrations of Pd precursor, octahedra (sample 6B) form. Interestingly, the addition of HCl to a synthesis facilitates the formation of octahedra at lower concentrations of Pd (*e.g.*, sample 4F *versus* sample 6B). All samples are prepared in good yield (>90%), and this observation is attributed to the use of a seed-mediated method. In fact, the high monodispersity contributes to the uniform assembly of many samples, with the cubic particles often adopting cubic packing (*e.g.*, sample 1B) and the cuboctahedral and octahedral particles often adopting hexagonally packed arrangements (*e.g.*, samples 4D and 5D, respectively).

Many samples were characterized in more detail to better understand the structural changes observed as well as to correlate the results with changes in the Au−Pd distribution in the final nanostructures. Shown in Figure S4 is a transmission electron microscopy (TEM) image and the corresponding electron diffraction (ED) of an individual octopodal nanocrystal oriented with four branches toward the TEM grid and four branches away (sample 4A). The square symmetry of the ED pattern indicates that the eight branches of the octopod grow along the ⟨111⟩ directions from the interior of the nanostructure, and the flattened tips correspond with the expression of {111} facets. Adding a sufficient amount of HCl to this overgrowth solution facilitated the formation of octahedral nanocrystals during co-reduction (sample 4F). ED of an individual particle is consistent with the octahedral shape (Figure S4). High magnification SEM images, structural models, TEM images, STEM images, and

elemental mapping by STEM energy dispersive X-ray (EDX) analysis of individual particles from row 4 are shown in Figure 2 from top to bottom. TEM and STEM-EDX elemental mapping provide remarkable insight into the changes in both morphology and composition that occur as a function of reaction pH. Palladium is dispersed all over the surface of the octopods and localizes along the tips of the branched nanostructures, with Au predominating in the interior of the particles (samples 4A and 4B; Pd-rich regions will appear lighter in TEM and STEM as $Z_{Au} > Z_{Pd}$). With decreasing pH, the SEM images reveal regions of negative curvature associated with the absence of {100} facets of what would otherwise be cuboctahedral particles (samples 4C and 4D). Structural models based on these SEM observations are provided in row 2. TEM and STEM-EDX mapping reveal again that the exteriors of the nanocrystals are Pd-rich. Interestingly, a core@shell Au@Pd particle structure is not obvious from microscopy analysis of the octahedral nanostructures (sample 4F), although it was initially assumed given the use of Au cores during synthesis and the tendency of Au precursors to reduce and deposit before Pd precursors. To our surprise, powder X-ray diffraction (XRD) of sample 4F indicates that the octahedra are primarily a Au-rich Au−Pd alloy (Figure S5). Note that according to the Au−Pd phase diagram, Au and Pd are soluble over a wide range of compositions.[36] Presumably this alloy exists as a shell on top of Au-based cores. Thus, controlling the kinetics of seed-mediated bimetallic deposition may represent a

general route to shape-controlled alloy nanocrystals. As is evident from the STEM-EDX elemental mapping, the shape of the Au-rich interior of the Au−Pd nanocrystals changes as a function of HCl addition, as does the distribution of Pd in the final nanocrystals. The chemical origin of these changes will be discussed in more detail later, but it is noted that there is very little variation in the Au:Pd ratio in the final nanostructures as a function of reaction pH (Table 1).

Similar characterization was conducted for nanocrystals formed as a function of Au:Pd precursor ratio with no HCl added to the overgrowth solution (column A). It is noted that there is a slight decrease in reaction pH down column A as the Pd precursor itself provides HCl to the reaction media; however, the change from one panel to the next is small compared to row 4 experiments, and similar structural changes are observed as a function of Au:Pd precursor ratio when the H_2PdCl_4 is replaced with Na_2PdCl_4 (see Table S1 and Figure S6). Shown in Figure 3 are TEM images and STEM-EDX elemental maps of individual particles from the samples in column A. As the amount of Pd precursor increases in the synthesis, the tips of the branches become substantially flattened. The STEM-EDX elemental maps indicate that these flattened tips are enriched with Pd relative to the rest of the nanostructure. The elemental maps also indicate that the branched nature of the Au-rich interior is generally maintained as a function of Au:Pd precursor ratio, unlike with the addition of HCl to the overgrowth solution. ED of sample 6A again indicates that branches of the octopods grow along the $\langle 111 \rangle$ directions of the core (Figure S4). Powder XRD of sample 6A indicates a complex composition composed of Au, Pd, and a Au−Pd alloy from the shoulder reflections at 38.2 and 40.1 degrees 2θ, consistent with diffraction from the Au and Pd {111} planes, respectively, and the broad reflection in between (Figure S5). Interestingly, the reflection at 40.1 degrees 2θ for Pd is not evident in the powder XRD pattern of sample 4A (Figure S5). Sample 4A is prepared with slightly less Pd precursor than sample 6A, and the width of the sheets terminating the branches of these octopods is also less than observed with sample 6A. This comparative analysis suggests that the Pd region is localized at the tips of the "sheeted" octopods. The amount of Pd in the final nanocrystals increases with increasing Pd precursor in the overgrowth solution as expected (Table 1). Taken with the results obtained at fixed Au:Pd precursor but different HCl contents, these findings illustrate that the Pd content and location can be predictably manipulated during seed-mediated co-reduction.

Additional experiments are still required to fully decouple the roles of HCl content and Au:Pd precursor ratio in morphology control. Mainly, it is important to consider the structure of the Au cores in nanocrystal formation, as the facets expressed and their internal twins can contribute to morphology development in seed-mediated syntheses.[29,37] Shown in Figure S7 is an SEM image of the Au cores used in this synthesis. They appear octahedral-like, with some particles showing rounded corners or minor protrusions. The use of single-crystalline octahedral-like cores is consistent with the final morphologies adopted by the Au−Pd nanocrystals. However, nanoparticles often restructure in solution in response to changes in their environment

TABLE 1. Ratio of Au:Pd (as X:1) in Various Nanocrystals As Obtained by EDX Analysis

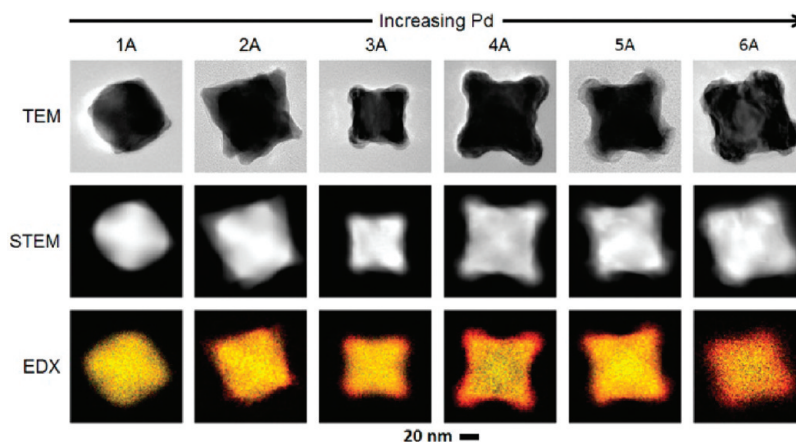| row 4	decreasing pH →					
	4A	4B	4C	4D	4E	4F
X	0.87	1.01	1.02	0.85	1.14	0.98
column A	increasing Pd →					
	1A	2A	3A	4A	5A	6A
X	19.7	3.55	1.73	0.87	0.40	0.28

Figure 3. From top to bottom, Au−Pd nanocrystals (column A, Figure 1) characterized by TEM, STEM, and STEM-EDX elemental mapping (yellow indicates Au and red indicates Pd).
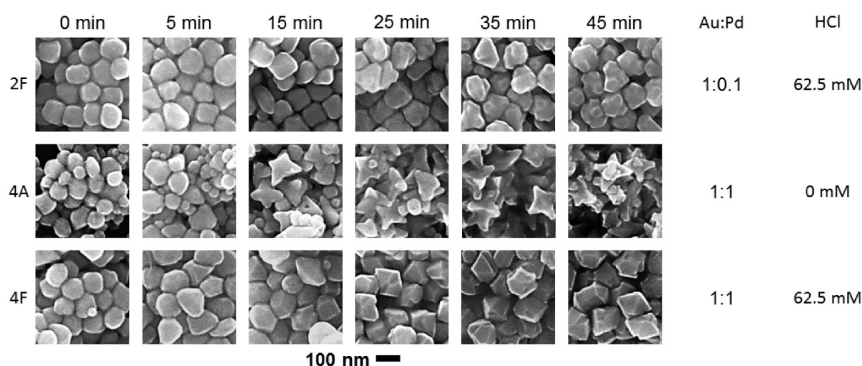
Figure 4. SEM images of the products obtained by analyzing aliquots at different times after the co-reduction step. From top to bottom: samples 2F, 4A, and 4F.

(*e.g.*, the addition of a capping agent).[38,39] It is possible that the addition of HCl to the overgrowth solution contributed to a change in core structure and in turn final nanostructure morphology. However, SEM analysis of Au cores exposed to HCl prior to the co-reduction step did not reveal any substantial changes in structure (Figure S7). Thus, the changes in final nanostructure morphology as a function of HCl do not arise from changes in core shape prior to co-reduction. Yet STEM-EDX elemental mapping of row 4 samples revealed Au-rich interiors of different shapes as a function of HCl content (Figure 2). At low HCl content (high pH) the Au-rich interiors are branched. Such structures are not favored by thermodynamics and typically form under conditions of fast growth, wherein metal deposition occurs at a faster rate than metal surface diffusion.[34] At higher HCl content (low pH) the Au-rich interiors are cuboctahedral or octahedral, which are thermodynamically more favored. These observations are consistent with the pH-dependent reducing capabilities of L-aa.[40] It is also noted that Au can be etched with Au(III)-CTAB complexes and that the rate of this oxidation is pH dependent, with points of high curvature being most susceptible to etching at low pH.[41] These two factors account for the different shapes observed in the Au-rich interiors of the Au–Pd nanocrystals as a function of HCl content, particularly as the addition of NaCl to the overgrowth solution rather than HCl did not facilitate similar morphology changes. Shown in Figure S8 are the results obtained when NaCl was added to the overgrowth solution rather than HCl, with all other synthetic conditions consistent with row 2 samples. High-quality octopodal structures were obtained at all concentrations. Finally, as the Pd precursor (H_2PdCl_4) provides HCl to the reaction media itself, it was replaced with Na_2PdCl_4 at the Au:Pd precursor ratio consistent with row 5 and the pH of the reaction media adjusted through the addition of HCl prior to co-reduction. The results are shown in Figure S6 and are similar to those obtained with H_2PdCl_4 as a function of reaction pH (A–F correspond to 2 mL of 0.0, 12.5, 25.0, 37.5, 50.0, and 62.5 mM HCl

added, respectively; the total reaction volume is 30.6 mL). Thus, the addition of HCl extraneously, not exclusively from the metal precursor, provides similar kinetic control of seed-mediated co-reduction. It is noted that adding a small amount of NaOH to the overgrowth solution also facilitated the formation of octopodal structures (Figure S9). This observation is consistent with branched nanostructures forming under fast growth conditions, as precursor reduction with L-aa is more facile at high pH.[40] Yet polydisperse quasi-spheres form at sufficiently high pH and may arise from uncontrolled precursor reduction and the decreased stability of the CTAB bilayers adsorbed to the surface of the growing nanocrystals (Figure S9).[40]

The discussed experiments highlight the important role of growth rate in morphology development. Time studies provide similar insight. Shown in Figure 4 are SEM images of the product obtained as a function of reaction time for samples 2F, 4A, and 4F. In the early stages of reaction all samples are ill-defined and reminiscent in form to the original Au cores. However, the morphologies of the nanostructures are similar to those shown in Figure 1 within 45 min and indicate that our sampling technique does not appreciably alter the growth processes. Interestingly, sample 2F adopts a "sheeted" octopodal morphology, but it does not appear to proceed through an octopodal intermediate without sheets, as one might interpret from Figure 1. Similarly, sample 4F adopts an octahedral-like morphology without proceeding through a branched morphology first. Yet octopodal structures form during the early stages of synthesis for sample 4A (15 min), which is prepared with less HCl in the overgrowth solution than sample 4F. This observation highlights the important role of reaction pH and fast growth in achieving branched nanocrystals. Otherwise, slow growth will predominate, as will convex structures. Significantly, these findings indicate that the different morphologies of the Au-rich phase formed initially during co-reduction direct the subsequent deposition of the Pd-rich phase.

Evaluation of Capping Agents. In addition to the important role of precursor reduction rate on morphology

development, structure direction can be achieved in a nanosynthesis through the use of capping agents (either intentionally added to the solution or present during a nanosynthesis from precursor selection).[38] In considering this seed-mediated co-reduction synthesis, the role of CTAB must be evaluated, as it is used as a stabilizing surfactant. CTAB is also used in Au nanorod syntheses, where it forms a bilayer, and the bromide is thought to electrostatically stabilize {100} facets relative to {111} facets given the prevalence of cube and rod-like structures prepared in its presence.[42−44] Thus, CTAB was replaced with cetyltrimethylammonium chloride (CTAC) to elucidate the role of Br$^-$ during the synthesis of Au−Pd nanocrystals *via* seed-mediated co-reduction. Note that the CTAB was replaced with CTAC after Au core formation but prior to co-reduction to ensure that any observed changes in morphology are from the change in surfactant and not the shape of the Au core (see Methods). CTAB and CTAC are both quaternary ammonium salts and differ only in their counteranion, Br$^-$ *versus* Cl$^-$. Interestingly, Mirkin and co-workers recently found that replacing CTAB with CTAC facilitated the formation of concave Au nanocubes rather than tetrahexahedra when all other synthetic parameters were held constant.[45] The origin of this difference was not elucidated but indicates that subtle changes in a synthesis can facilitate unique outcomes. Shown in Figure 5A and B are comparative SEM images of the Au−Pd nanostructures formed at a 1:0.1 Au:Pd precursor ratio in the presence of equal concentrations of CTAC and CTAB, respectively. Octopods form in both cases. Yet the tips of the octopods prepared in the presence of CTAC are much sharper than those prepared with CTAB, which display flattened tips corresponding to Pd-rich {111} facets. Adding KBr to the CTAC system led to the expression of similarly flattened tips at low concentrations (CTAC:Br$^-$ = 1:0.75; Figure 5C).

It is curious that Pd-rich {111} facets are widened with increasing Br$^-$ content rather than {100} facets expressed. We interpret this observation to mean that the addition of Br$^-$ to the synthesis has its greatest effect on Pd precursor reduction rather than habit modification *via* surface stabilization or the reduction properties of the Au precursor. It is known that Pd(II) can coordinate as $[CTA]_2PdBr_4$ and related species and that the reduction rate associated with $[PdBr_4]^{2-}$ is slow relative to $[PdCl_4]^{2-}$.[30] This condition could provide greater temporal separation between the reduction of the Au and Pd precursors. The association of Pd(II) with Br$^-$ in our system was verified *via* UV−visible spectroscopy (see Figure S10). On the basis of these findings, we believe that adding Br$^-$ to the synthesis temporally separates reduction of the Au and Pd precursors and, in turn, their addition to the growing nanostructures. We note that the Au precursor may be similarly coordinated with Br$^-$, but the
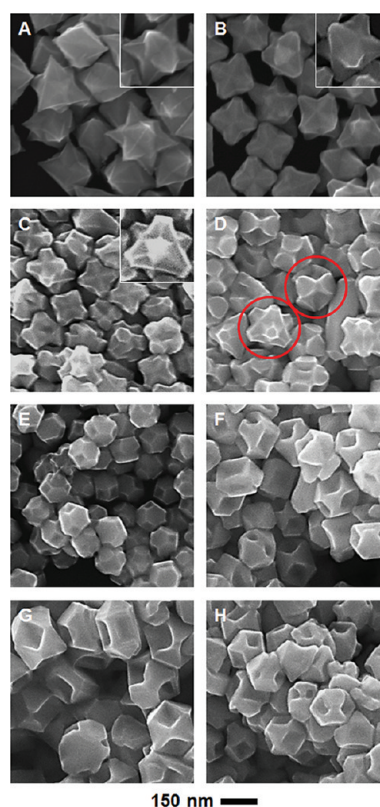

Figure 5. SEM images of Au−Pd nanocrystals formed *via* seed-mediated co-reduction at a Au:Pd precursor ratio of 1:0.1. (A) CTAC and (B) CTAB were used as stabilizing agents, respectively. The concentration of CTA$^+$ is the same (see Methods, Hopper-like Nanocrystal Formation). KBr solution was added to the CTAC-based synthesis prior to co-reduction at CTAC-to-Br$^-$ ratios of 1:X where X is (C) 0.75, (D) 0.875, (E) 1.0, (F) 1.125, (G) 1.25, and (H) 1.375. A low concentration of HCl was added to the syntheses of samples (C)−(H), as it improved sample monodispersity (see Methods and Figure S8 for control experiment). Circled in (D) are two different particle architectures, where one particle has {111} facets that have fused together to generate a hopper-like nanocrystal and the other does not.

observation of Au-based branches suggests that the kinetics of its reduction are not as strongly influenced by this factor. Regardless, temporally separating the reduction of different precursors would lead to the spatial separation of Au-rich and Pd-rich regions in the final nanostructures at sufficiently high Br$^-$ concentrations.

As the amount of Br$^-$ in the syntheses increases further, the nanocrystals adopt octapodal structures with truncated tips that in some cases appear fused together (CTAC:Br$^-$ = 1:0.875; Figure 5D). Remarkably, at even higher Br$^-$ concentrations, the {111} tips are so wide that nanocrystals form with deep angular concavities on what would be the {100} facets of cuboctahedral nanocrystals otherwise (Figure 5E−H). Control experiments found that adding more Br$^-$ to the traditional CTAB-based synthesis of octopods facilitated the formation of similar structures (Figure S11A), while adding additional Cl$^-$ to the bromide-free/CTAC synthesis gave sharply tipped octopods (Figure S11B).

These concave crystals bear a resemblance to hopper crystals, which contain face-centered pits and whose name derives from the railway cars that carry grain.[46−49] Such crystals form under kinetically controlled growth conditions wherein crystal edges grow faster than crystal faces. However, in our system no concavities are observed within the {111} facets, as would be expected from such overgrowth of cuboctahedra, and suggests that a different growth mechanism is operating.[49] Interestingly, Mirkin and co-workers recently reported the Ag^+-mediated synthesis of Au octahedra with deep angular concavities similar to those observed in our Au−Pd hopper-like nanocrystals.[50] They attributed the formation of their structures to slowed precursor reduction and kinetically controlled growth conditions that favor metal deposition on the highest energy features, as is observed here as well. Additional characterization is provided in Figure 6. A STEM image of an individual hopper-like particle reveals that the {111} facets on opposite sides of the crystal are both truncated triangles but rotated 45° from one another. STEM-EDX elemental mapping indicates that Pd is dispersed all over the surface with the structure consisting of a Au-based cuboctahedral core.

From this detailed analysis, it is evident that morphology development during seed-mediated co-reduction is sensitive to factors that influence growth kinetics. A complicating factor of this analysis is that each metal precursor can respond differently to synthetic parameters that govern kinetics. In our Au−Pd system, reaction pH had its greatest effect in directing the growth of the Au-rich phase and thus its shape. This observation can be accounted for by the pH-dependent rates of (i) metal precursor reduction with L-aa and (ii) Au core etching via Au(III)-CTAB complexes. Interestingly, revisiting the results presented in Figure S3 reveals a similar pH dependence for the seed-mediated growth of Au nanostructures. Gold cuboctahedra, Au nanocubes, and a mixture of Au nanocubes and octahedra form with increasing HCl content in the overgrowth solution containing only Au precursor. In contrast, the reduction of only Pd precursor yields {111}-terminated Au@Pd octahedra with increasing HCl content in the overgrowth solution. The different behaviors observed in the Au and Pd systems manifest in the bimetallic system as well, with the Au-rich regions adopting an assortment of shapes dependent on pH and the Pd-rich regions expressing {111} facets. Thus, studying the trends observed in monometallic nanocrystal syntheses may facilitate the predictive synthesis of bimetallic nanostructures via seed-mediated co-reduction.

Optical Properties of Au−Pd Nanocrystals. On account of their unique structures, various samples were also characterized by UV−visible spectroscopy. Anisotropic nanocrystals composed of Au, including branched nanostars and 1-D nanorods, have attracted much attention on account of their tunable SPRs in the visible
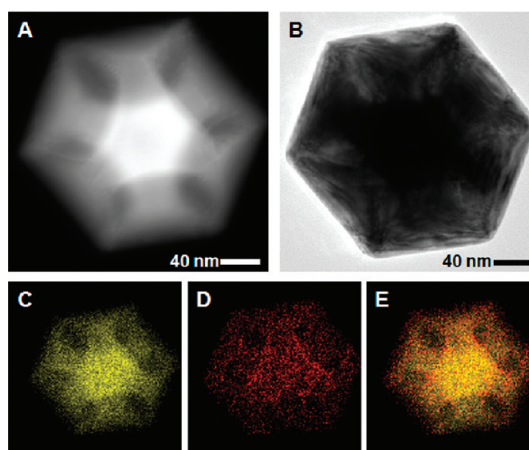

Figure 6. (A) STEM and (B) TEM images of a hopper-like nanocrystal as prepared in Figure 5G. The nanocrystal was also characterized using STEM-EDX elemental mapping: (C) Au only, (D) Pd only, and (E) an overlay of the Au and Pd signals.

and near-IR region.[40,51,52] This region is of technological relevance for biomedical applications and chemical sensing modalities via Raman spectroscopy.[53] Much less is known about the optical properties of such structures when they incorporate a second metal, such as Pd. However, studies of Au@Pd nanobars show that layers of Pd blue shift and broaden the LSPR on account of the difference in dielectric constant between Au and Pd and increased damping from the Pd shell.[54] The normalized UV−visible spectra for the Au−Pd nanocrystals in row 4 are shown in Figure 7A, with the primary area of interest enlarged in Figure 7B. The SPR for sample 4A is located at 700 nm. This SPR position in the near-IR is consistent with the branched nature of the Au−Pd nanocrystals.[51] Recall that adding HCl to the overgrowth solution yielded nanocrystals of similar size but with decreasing branch length and flattened tips. These changes in morphology are correlated with a blue shift to 400 nm, followed by slight red shifts to ∼550 nm as the nanocrystals adopt an octahedral shape. These observations are consistent with studies of other branched structures wherein a decrease in branch length manifested initially as a blue shift.[51] The resonance associated with sample 4F is slightly to the blue compared to octahedral Au nanocrystals of similar size and is the result of Pd on the surface of the nanocrystal.

The UV−visible spectra are presented in Figure 7C for the Au−Pd octopods with different Pd loadings at their tips (column A). A sharp SPR is observed at 600 nm for sample 1A. There is a gradual red shift with increasing Pd precursor in the overgrowth solution (samples 2A through 4A) followed by a blue shift to 500 nm with sample 6A. Given the structural similarities between all of the samples, the position of the SPR was analyzed as a function of both branch length and tip width for the Au−Pd octopods (Figure 7D and E). This analysis found that the red shift arises primarily with an elongation in
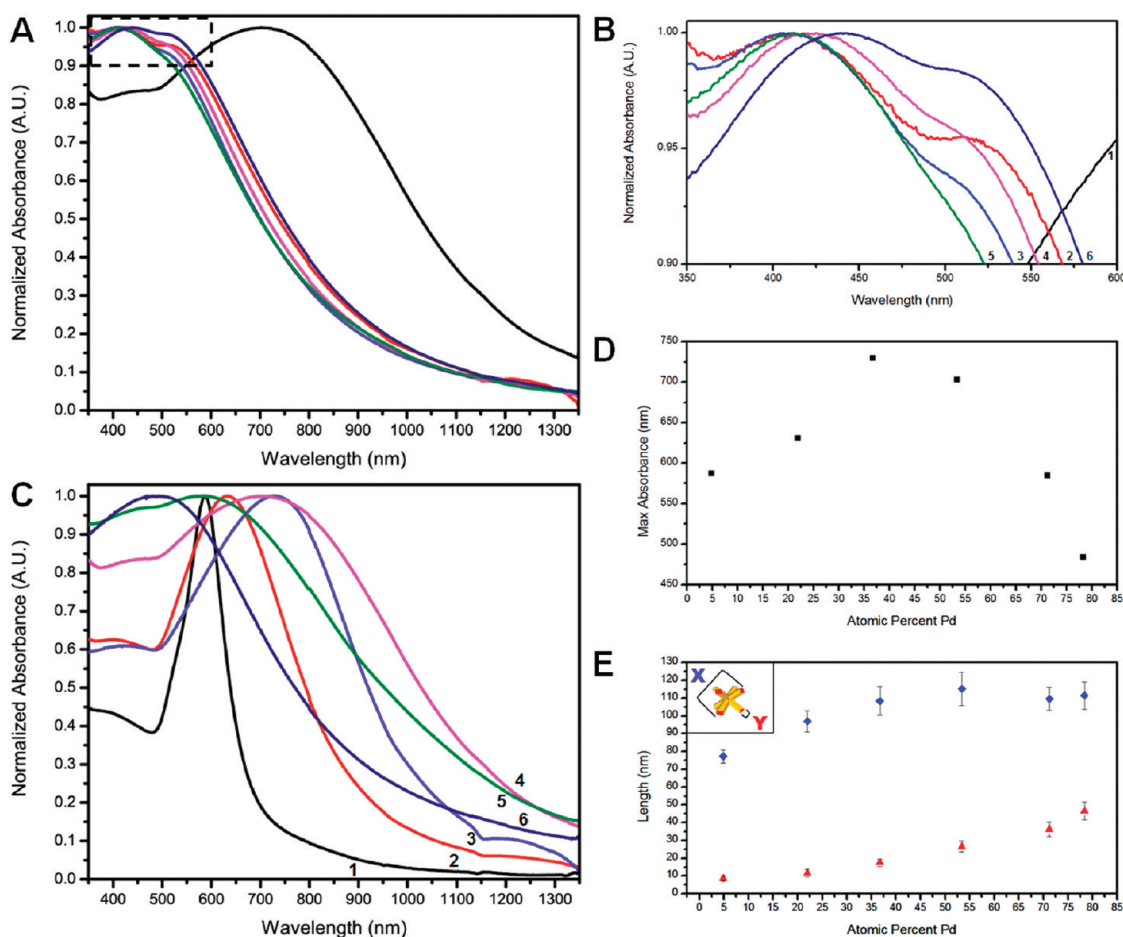
Figure 7. (A) Normalized absorbance spectra of Au−Pd nanocrystals (row 4, Figure 1) and (B) inset of the spectra with labels 1−6 corresponding to samples 4A−4F, respectively. (C) Normalized absorbance spectra of Au−Pd nanocrystals (column A, Figure 1) with labels 1−6 corresponding to samples 1A−6A, respectively. (D) Wavelength of maximum SPR absorbance and (E) corresponding dimensions of the nanocrystals (column A, Figure 1) plotted as a function of atomic percent Pd in the synthesis.

branch length denoted as "X" in Figure 7E, which increases consistently for samples 1A−4A (Figure 7E). On the other hand, the blue shift correlates with an increase in tip width denoted as "Y" in Figure 7E, which increases most for samples 4A−6A (Figure 7E). Eluci-dating the synthetic parameters that govern structure formation allows for the optical properties of these Au−Pd nanocrystals to be facilely and predictably manipulated *via* seed-mediated co-reduction.

CONCLUSIONS

The synthesis of bimetallic nanostructures with de-fined features is often daunting with traditional co-reduction methods on account of the different proper-ties of each metal precursor. Yet as demonstrated here, coupling co-reduction with a seed-mediated synthesis

represents a versatile route to architecturally controlled bimetallic nanostructures with Au−Pd octopods, con-cave nanostructures including new hopper-like nano-crystals with deep angular concavities, and shape-controlled alloy nanocrystals achieved. Our systematic study of the reaction conditions attributes the formation of these distinct nanostructures to the careful manipula-tion of growth kinetics, with observations in the bime-tallic system being similar to those in the monometallic analogues. As such, seed-mediated co-reduction repre-sents a potentially powerful means of achieving bime-tallic nanostructures with well-defined and controllable features. Also, these results provide insight into how self-seeding co-reduction techniques could be exploited to achieve one-step approaches toward architecturally con-trolled bimetallic nanostructures.[55−57]

METHODS

Chemicals. L-Ascorbic acid ($C_6H_8O_6$, 99%), palladium(II) chloride ($PdCl_2$, 99.98%), chloroauric acid ($HAuCl_4 \cdot 3H_2O$, 99.9%), cetyltrimethylammonium bromide (CTAB, 98%, lot #'s:

050M01711 V and 120M01411 V), cetyltrimethylammonium chloride (CTAC, 0.78M, lot #'s: MKBB4924 and STBC2574), sodium chloride (NaCl, 99%), potassium bromide (KBr, 99%), and sodium borohydride ($NaBH_4$, 98.5%) were used as purchased

from Sigma Aldrich. Sodium hydroxide (NaOH, 97%) was used as purchased from EMD. Aqueous, concentrated hydrochloric acid (12.1M) was purchased from Mallinckrodt. Nanopure water (18.2 MΩ·cm) was used in all experiments. An aqueous 10 mM H_2PdCl_4 solution was prepared by heating at ~70 °C and stirring dissolved $PdCl_2$ (44.6 mg) in 25 mL of HCl (pH 1.69) for 1 h.

Gold Nanoparticle Seeds. To make the initial Au seeds, 4 mL of water and then 1 mL of $HAuCl_4$ (2.5 mM) solution were added to 5 mL of CTAB (150 mM) solution in a 30 mL reaction vial. A 0.6 mL amount of an ice-cold $NaBH_4$ (10 mM) solution was added immediately with vigorous stirring, forming a clear brown solution. This solution was capped and allowed to stir slowly at room temperature for 3 h. A 0.2 mL aliquot was then diluted with 19.8 mL of water. The seeds were aged at room temperature and used after 3 days to prepare Au cores for Au—Pd nanocrystal formation.

Gold Nanoparticle Cores. To synthesize the Au cores, 0.1 mL of $HAuCl_4$ (9 mM) solution was added to 2 mL of CTAB (0.2 M) solution followed immediately by 1.5 mL of ascorbic acid (0.1 M) solution. This solution was immediately diluted to 25 mL with H_2O followed promptly by adding 1.0 mL of the seed solution. This reaction vial was capped and allowed to sit undisturbed in a 25 °C oil bath for 24 h.

Gold—Palladium Nanocrystal Formation. To prepare the various Au—Pd nanocrystals, 2 mL of either water or HCl acid solution (concentration denoted in the text and Table S1) was added to the entire Au core solution. This procedure was followed by the simultaneous addition *via* separate pipettes of 2 mL of H_2PdCl_4 and 0.1 mL of $HAuCl_4$ solution (concentrations denoted in the text and Table S1). The vials were gently mixed by inversion followed promptly by the addition of 0.5 mL of ascorbic acid (0.1 M) solution. The reaction vial was capped and allowed to sit undisturbed in a 25 °C oil bath for 24 h. It is noted that HCl solutions were prepared by diluting concentrated HCl (12.1 M) to the desired concentration and checking the solution pH (included in Table S2). The H_2PdCl_4 solution was similarly prepared by dilution of the 10 mM H_2PdCl_4 solution described under Chemicals.

Control Experiments with Sodium Chloride or Sodium Hydroxide. NaCl or NaOH was substituted for HCl at the acid addition step using identical concentrations (as denoted in Table S1). Otherwise, the experimental procedure was identical to that used for Au—Pd nanocrystal formation.

Hopper-Like Nanocrystal Formation. The Au core solution, as prepared earlier, was spun down by centrifugation, and the supernatant—containing the dissolved CTAB used in preparation—was removed by decantation. The Au cores were then resuspended in water to 1 mL for later use. One milliliter of a KBr solution (varying concentrations: 0.30, 0.35, 0.40, 0.45, 0.50, and 0.55 M as denoted in the text) was added to a 1 mL solution of 0.4 M CTAC. To this solution were added sequentially 0.1 mL of a 200 mM $HAuCl_4$ solution and 0.2 mL of a 10 mM H_2PdCl_4 solution (Au:Pd = 1:0.1), followed by 1.5 mL of a 0.2 M ascorbic acid solution. Depending on the synthesis, 2 mL of water or 25 mM HCl solution was then added, as denoted in the text. The HCl improved sample homogeneity. Finally, this solution was diluted to 25 mL using Nanopure water, then 1 mL of the core solution was added.

Characterization. Images of the nanoparticles were taken *via* a FEI Quanta 600F Environmental scanning electron microscope operated at 30 kV and a spot size of 3. The composition of the nanoparticles was determined with an Oxford INCA energy dispersive X-ray detector interfaced to the SEM operated at 30 kV. STEM/TEM images were taken on a JEOL JEM 3200FS transmission electron microscope at 300 kV and a spot size of 1 with a Gatan 4k × 4k Ultrascan 4000. Energy dispersive X-ray spectra were obtained with an Oxford INCA dispersive X-ray system interfaced to the JEM 3200FS TEM, operating at 300 kV. Samples for TEM analysis were prepared by washing a copper-coated carbon grid with chloroform to remove Formvar, then drop-casting a dispersed particle solution onto the grid. Samples for SEM and EDX analysis were prepared by drop-casting a dispersed particle solution onto a silicon wafer and then washing the wafer twice with methanol after initial solvent evaporation. The optical properties of various samples were measured with a Varian CARY 5000 Bio UV—visible spectrophotometer, using a quartz cuvette and a background scan of water. Samples for powder XRD were deposited on amorphous glass slides and analyzed with Siemens/Bruker D-5000 using Cu Kα radiation (λ = 0.15418 nm).

Conflict of Interest: The authors declare no competing financial interest.

Supporting Information Available: Electron diffraction and powder XRD measurements, pH and precursor concentration tables, as well as results from control experiments are available free of charge *via* the Internet at http://pubs.acs.org.

REFERENCES AND NOTES

1. Wang, D.; Li, Y. Bimetallic Nanocrystals: Liquid-Phase Synthesis and Catalytic Applications. *Adv. Mater.* **2011**, *23*, 1044–1060.

2. Skrabalak, S. E.; Xia, Y. Pushing Nanocrystal Synthesis toward Nanomanufacturing. *ACS Nano* **2009**, *3*, 10–15.

3. González, E.; Arbiol, J.; Puntes, V. F. Carving at the Nanoscale: Sequential Galvanic Exchange and Kirkendall Growth at Room Temperature. *Science* **2011**, *334*, 1377–1380.

4. Hong, J. W.; Kim, D.; Lee, Y. W.; Kim, M.; Kang, S. W.; Han, S. W. Atomic-Distribution-Dependent Electrocatalytic Activity of Au—Pd Bimetallic Nanocrystals. *Angew. Chem., Int. Ed.* **2011**, *50*, 8876–8880.

5. Wang, L.; Nemoto, Y.; Yamauchi, Y. Direct Synthesis of Spatially-Controlled Pt-on-Pd Bimetallic Nanodendrites with Superior Electrocatalytic Activity. *J. Am. Chem. Soc.* **2011**, *133*, 9674–9677.

6. Ataee-Esfahani, H.; Wang, L.; Nemoto, Y.; Yamauchi, Y. Synthesis of Bimetallic Au@Pt Nanoparticles with Au Core and Nanostructured Pt Shell toward Highly Active Electrocatalysts. *Chem. Mater.* **2010**, *22*, 6310–6318.

7. Yin, A.-X.; Min, X.-Q.; Zhang, Y.-W.; Yan, C.-H. Shape-Selective Synthesis and Facet-Dependent Enhanced Electrocatalytic Activity and Durability of Monodisperse Sub-10 nm Pt-Pd Tetrahedrons and Cubes. *J. Am. Chem. Soc.* **2011**, *133*, 3816–3819.

8. Zhang, H.; Jin, M.; Liu, H.; Wang, J.; Kim, M. J.; Yang, D.; Xie, Z.; Liu, J.; Xia, Y. Facile Synthesis of Pd—Pt Alloy Nanocages and Their Enhanced Performance for Preferential Oxidation of CO in Excess Hydrogen. *ACS Nano* **2011**, *5*, 8212–8222.

9. Cortie, M. B.; McDonagh, A. M. Synthesis and Optical Properties of Hybrid and Alloy Plasmonic Nanoparticles. *Chem. Rev.* **2011**, *111*, 3713–3735.

10. Major, K.; De, C.; Obare, S. Recent Advances in the Synthesis of Plasmonic Bimetallic Nanoparticles. *Plasmonics* **2009**, *4*, 61–78.

11. Xia, Y. N.; Li, W. Y.; Cobley, C. M.; Chen, J. Y.; Xia, X. H.; Zhang, Q.; Yang, M. X.; Cho, E. C.; Brown, P. K. Gold Nanocages: From Synthesis to Theranostic Applications. *Acc. Chem. Res.* **2011**, *44*, 914–924.

12. Liu; Guyot-Sionnest, P. Synthesis and Optical Characterization of Au/Ag Core/Shell Nanorods. *J. Phys. Chem. B* **2004**, *108*, 5882–5888.

13. Becker, J.; Zins, I.; Jakab, A.; Khalavka, Y.; Schubert, O.; Sönnichsen, C. Plasmonic Focusing Reduces Ensemble Linewidth of Silver-Coated Gold Nanorods. *Nano Lett.* **2008**, *8*, 1719–1723.

14. Seo, D.; Il Yoo, C.; Jung, J.; Song, H. Ag-Au-Ag Heterometallic Nanorods Formed through Directed Anisotropic Growth. *J. Am. Chem. Soc.* **2008**, *130*, 2940–2941.

15. Zhou, S. H.; Jackson, G. S.; Eichhorn, B. AuPt Alloy Nanoparticles for CO-Tolerant Hydrogen Activation: Architectural Effects in Au-Pt Bimetallic Nanocatalysts. *Adv. Funct. Mater.* **2007**, *17*, 3099–3104.

16. Ortiz, N.; Skrabalak, S. E. Controlling the Growth Kinetics of Nanocrystals *via* Galvanic Replacement: Synthesis of Au Tetrapods and Star-Shaped Decahedra. *Cryst. Growth Des.* **2011**, *11*, 3545–3550.

17. Niu, W.; Zhang, L.; Xu, G. Shape-Controlled Synthesis of Single-Crystalline Palladium Nanocrystals. *ACS Nano* **2010**, *4*, 1987–1996.

18. Habas, S. E.; Lee, H.; Radmilovic, V.; Somorjai, G. A.; Yang, P. Shaping Binary Metal Nanocrystals through Epitaxial Seeded Growth. *Nat. Mater.* **2007**, *6*, 692–697.

19. Carbone, L.; Cozzoli, P. D. Colloidal Heterostructured Nanocrystals: Synthesis and Growth Mechanisms. *Nano Today* **2010**, *5*, 449–493.

20. Fan, F. R.; Liu, D. Y.; Wu, Y. F.; Duan, S.; Xie, Z. X.; Jiang, Z. Y.; Tian, Z. Q. Epitaxial Growth of Heterogeneous Metal Nanocrystals: From Gold Nano-Octahedra to Palladium and Silver Nanocubes. *J. Am. Chem. Soc.* **2008**, *130*, 6949–6951.

21. Banin, U. Tiny Seeds Make a Big Difference—A Seeded-Growth Approach Provides Shape-Controlled Bimetallic Nanocrystals and Opens the Way for a Rich Selection of New Nanoscale Building Blocks. *Nat. Mater.* **2007**, *6*, 625–626.

22. Sau, T. K.; Murphy, C. J. Room Temperature, High-Yield Synthesis of Multiple Shapes of Gold Nanoparticles in Aqueous Solution. *J. Am. Chem. Soc.* **2004**, *126*, 8648–8649.

23. Lu, C.-L.; Prasad, K. S.; Wu, H.-L.; Ho, J. A.; Huang, M. H. Au Nanocube-Directed Fabrication of Au—Pd Core—Shell Nanocrystals with Tetrahexahedral, Concave Octahedral, and Octahedral Structures and Their Electrocatalytic Activity. *J. Am. Chem. Soc.* **2010**, *132*, 14546–14553.

24. Yu, Y.; Zhang, Q.; Liu, B.; Lee, J. Y. Synthesis of Nanocrystals with Variable High-Index Pd Facets through the Controlled Heteroepitaxial Growth of Trisoctahedral Au Templates. *J. Am. Chem. Soc.* **2010**, *132*, 18258–18265.

25. Yang, C.-W.; Chanda, K.; Lin, P.-H.; Wang, Y.-N.; Liao, C.-W.; Huang, M. H. Fabrication of Au—Pd Core—Shell Heterostructures with Systematic Shape Evolution Using Octahedral Nanocrystal Cores and Their Catalytic Activity. *J. Am. Chem. Soc.* **2011**, *133*, 19993–20000.

26. Wang, F.; Li, C.; Sun, L.-D.; Wu, H.; Ming, T.; Wang, J.; Yu, J. C.; Yan, C.-H. Heteroepitaxial Growth of High-Index-Faceted Palladium Nanoshells and Their Catalytic Performance. *J. Am. Chem. Soc.* **2010**, *133*, 1106–1111.

27. DeSantis, C. J.; Peverly, A. A.; Peters, D. G.; Skrabalak, S. E. Octopods *versus* Concave Nanocrystals: Control of Morphology by Manipulating the Kinetics of Seeded Growth *via* Co-Reduction. *Nano Lett.* **2011**, *11*, 2164–2168.

28. Kim, D.; Lee, Y. W.; Lee, S. B.; Han, S. W. Convex Polyhedral Au@Pd Core—Shell Nanocrystals with High-Index Facets. *Angew. Chem., Int. Ed.* **2012**, *51*, 159–163.

29. Xia, Y. N.; Xiong, Y. J.; Lim, B.; Skrabalak, S. E. Shape-Controlled Synthesis of Metal Nanocrystals: Simple Chemistry Meets Complex Physics? *Angew. Chem., Int. Ed.* **2009**, *48*, 60–103.

30. Berhault, G.; Bausach, M.; Bisson, L.; Becerra, L.; Thomazeau, C.; Uzio, D. Seed-Mediated Synthesis of Pd Nanocrystals: Factors Influencing a Kinetic- or Thermodynamic-Controlled Growth Regime. *J. Phys. Chem. C* **2007**, *111*, 5915–5925.

31. Okitsu, K.; Sharyo, K.; Nishimura, R. One-Pot Synthesis of Gold Nanorods by Ultrasonic Irradiation: The Effect of pH on the Shape of the Gold Nanorods and Nanoparticles. *Langmuir* **2009**, *25*, 7786–7790.

32. Goia, D. V.; Matijevic, E. Tailoring the Particle Size of Monodispersed Colloidal Gold. *Colloid Surf., A* **1999**, *146*, 139–152.

33. Trigari, S.; Rindi, A.; Margheri, G.; Sottini, S.; Dellepiane, G.; Giorgetti, E. Synthesis and Modelling of Gold Nanostars with Tunable Morphology and Extinction Spectrum. *J. Mater. Chem.* **2011**, *21*, 6531–6540.

34. Watt, J.; Cheong, S.; Toney, M. F.; Ingham, B.; Cookson, J.; Bishop, P. T.; Tilley, R. D. Ultrafast Growth of Highly Branched Palladium Nanostructures for Catalysis. *ACS Nano* **2010**, *4*, 396–402.

35. Cheong, S.; Watt, J.; Ingham, B.; Toney, M. F.; Tilley, R. D. *In Situ* and *Ex Situ* Studies of Platinum Nanocrystals: Growth and Evolution in Solution. *J. Am. Chem. Soc.* **2009**, *131*, 14590–14595.

36. Massalski, T. B. *Binary Alloy Phase Diagrams*, 2nd ed.; Okamoto, H., Subramanian, P. R., Kacprzak, L., Eds.; ASM Int.: Materials Park, OH, 1990.

37. Tsuji, M.; Miyamae, N.; Lim, S.; Kimura, K.; Zhang, X.; Hikino, S.; Nishio, M. Crystal Structures and Growth Mechanisms of Au@Ag Core—Shell Nanoparticles Prepared by the Microwave—Polyol Method. *Cryst. Growth Des.* **2006**, *6*, 1801–1807.

38. Zeng, J.; Zheng, Y. Q.; Rycenga, M.; Tao, J.; Li, Z. Y.; Zhang, Q. A.; Zhu, Y. M.; Xia, Y. N. Controlling the Shapes of Silver Nanocrystals with Different Capping Agents. *J. Am. Chem. Soc.* **2010**, *132*, 8552–8553.

39. Narayanan, R.; El-Sayed, M. A. Catalysis with Transition Metal Nanoparticles in Colloidal Solution: Nanoparticle Shape Dependence and Stability. *J. Phys. Chem. B* **2005**, *109*, 12663–12676.

40. Bullen, C.; Zijlstra, P.; Bakker, E.; Gu, M.; Raston, C. Chemical Kinetics of Gold Nanorod Growth in Aqueous CTAB Solutions. *Cryst. Growth Des.* **2011**, *11*, 3375–3380.

41. Rodríguez-Fernández, J.; Pérez-Juste, J.; Mulvaney, P.; Liz-Marzán, L. M. Spatially-Directed Oxidation of Gold Nanoparticles by Au(III)—CTAB Complexes. *J. Phys. Chem. B* **2005**, *109*, 14257–14261.

42. Murphy, C. J.; Thompson, L. B.; Alkilany, A. M.; Sisco, P. N.; Boulos, S. P.; Sivapalan, S. T.; Yang, J. A.; Chernak, D. J.; Huang, J. The Many Faces of Gold Nanorods. *J. Phys. Chem. Lett.* **2010**, *1*, 2867–2875.

43. Murphy, C. J.; Sau, T. K.; Gole, A. M.; Orendorff, C. J.; Gao, J.; Gou, L.; Hunyadi, S. E.; Li, T. Anisotropic Metal Nanoparticles: Synthesis, Assembly, and Optical Applications. *J. Phys. Chem. B* **2005**, *109*, 13857–13870.

44. Xiong, Y. J.; Cai, H. G.; Wiley, B. J.; Wang, J. G.; Kim, M. J.; Xia, Y. N. Synthesis and Mechanistic Study of Palladium Nanobars and Nanorods. *J. Am. Chem. Soc.* **2007**, *129*, 3665–3675.

45. Zhang, J.; Langille, M. R.; Personick, M. L.; Zhang, K.; Li, S.; Mirkin, C. A. Concave Cubic Gold Nanocrystals with High-Index Facets. *J. Am. Chem. Soc.* **2011**, *132*, 14012–14014.

46. Zhu, J. P.; Yu, S. H.; He, Z. B.; Jiang, J.; Chen, K.; Zhou, X. Y. Complex PbTe Hopper (Skeletal) Crystals with High Hierarchy. *Chem. Commun.* **2005**, 5802–5804.

47. Zhang, J.; Zhang, S.; Wang, Z.; Zhang, Z.; Wang, S.; Wang, S. Hopper-Like Single Crystals of Sodium Chloride Grown at the Interface of Metastable Water Droplets. *Angew. Chem., Int. Ed.* **2011**, *50*, 6044–6047.

48. Dickinson, S. R.; McGrath, K. M. Switching between Kinetic and Thermodynamic Control: Calcium Carbonate Growth in the Presence of a Simple Alcohol. *J. Mater. Chem.* **2003**, *13*, 928–933.

49. Murray, B. J.; Li, O.; Newberg, J. T.; Menke, E. J.; Hemminger, J. C.; Penner, R. M. Shape- and Size-Selective Electrochemical Synthesis of Dispersed Silver(I) Oxide Colloids. *Nano Lett.* **2005**, *5*, 2319–2324.

50. Langille, M. R.; Personick, M. L.; Zhang, J.; Mirkin, C. A. Bottom-Up Synthesis of Gold Octahedra with Tailorable Hollow Features. *J. Am. Chem. Soc.* **2011**, *133*, 10414–10417.

51. Kim, D. Y.; Yu, T.; Cho, E. C.; Ma, Y.; Park, O. O.; Xia, Y. Synthesis of Gold Nano-hexapods with Controllable Arm Lengths and Their Tunable Optical Properties. *Angew. Chem., Int. Ed.* **2011**, *50*, 6328–6331.

52. Kumar, P. S.; Pastoriza-Santos, I.; Rodriguez-Gonzalez, B.; Garcia de Abajo, F. J.; Liz-Marzan, L. M. High-Yield Synthesis and Optical Response of Gold Nanostars. *Nanotechnology* **2008**, *19*, 015606.

53. Willets, K. A.; Van Duyne, R. P. Localized Surface Plasmon Resonance Spectroscopy and Sensing. *Annu. Rev. Phys. Chem.* **2007**, *58*, 267–297.

54. Zhang, K.; Xiang, Y.; Wu, X.; Feng, L.; He, W.; Liu, J.; Zhou, W.; Xie, S. Enhanced Optical Responses of Au@Pd Core/Shell Nanobars. *Langmuir* **2008**, *25*, 1162–1168.

55. Wang, L.; Yamauchi, Y. Autoprogrammed Synthesis of Triple-Layered Au@Pd@Pt Core-Shell Nanoparticles Consisting of a Au@Pd Bimetallic Core and Nanoporous Pt Shell. *J. Am. Chem. Soc.* **2010**, *132*, 13636–13638.

56. Jiang, X.; Zeng, Q.; Yu, A. A Self-Seeding Coreduction Method for Shape Control of Silver Nanoplates. *Nanotechnology* **2006**, *17*, 4929–4935.

57. Sun, Y.; Xia, Y. Large-Scale Synthesis of Uniform Silver Nanowires Through a Soft, Self-Seeding, Polyol Process. *Adv. Mater.* **2002**, *14*, 833–837.